Determination of geometrical parameters of the microstructure of a porous medium Application to cementitious materials

Khaled Bourbatache, Fares Bennai, C.-F. Zhao, O. Millet, Abdelkarim Aît-Mokhtar

Determination of geometrical parameters of the microstructure of a porous medium: application to cementitious materials.

Mohamed Khaled Bourbatache[a,d], Fares Bennai[b], Chao-Fa Zhao[c], Olivier Millet[d], Abdelkarim Aït-Mokhtar[d]

[a] *LGCGM EA 3913, INSA Rennes, 20 Avenue des Buttes de Coesmes, 35700 Rennes, France.*
[b] *University of Lorraine, CNRS, Arts et métiers ParisTech, LEM3, 57000 Metz, France.*
[c] *Faculty of Engineering Technology, University of Twente, Enschede, The Netherlands.*
[d] *LaSIE - UMR CNRS 7356, University of La Rochelle, Avenue Michel Crépeau 17042 La Rochelle Cedex 1, France.*

Abstract

Mass transfer in porous media is governed, besides the species diffusion coefficient, by the porosity and the geometrical parameters of the materials microstructure. This paper aims at developing a methodology for the determination of tortuosity and constrictivity factor based on a diffusion modeling in a porous medium of neutral species. Tortuosity was obtained by the computation of particles trajectory. After which, constrictivity was deduced from the formation factor, represented by the relative diffusion coefficient. Results show that tortuosity evolves in the opposite direction that the porosity while constrictivity evolves in the same direction. In addition, both parameters further slowdown the transfer for lower porosities.

Keywords: Tortuosity, Porosity, Constrictivity, Homogenization, Specific surface.

*Corresponding author
Email address: mohamed-khaled.bourbatache@insa-rennes.fr (Mohamed Khaled Bourbatache)

Preprint submitted to International Communications in Heat and Mass Transfer July 21, 2020

Nomenclature

δ	Constrictivity of the porous medium
Γ	Microscopic boundary of Ω
Γ_{ff}	Fluid-fluid interface
Γ_{sf}	Solid-fluid interface
$\boldsymbol{\chi}$	Local variable
Ω	Microscopic domain
Ω_f	Fluid phase of Ω
Ω_s	Solid phase of Ω
σ	Standard deviation
τ	Tortuosity of the porous medium
φ	Porosity of the porous medium
Δ_y	Laplacien operator according to the microscopic coordinates
$\langle \cdot \rangle$	Average operator upon Ω
$(\cdot)^T$	Transposition operator
$\overline{\cdot}$	Arithmetic mean of $\cdot$
div_y	Divergence operator according to the microscopic coordinates
$\mathbf{D}^{hom}$	Homogenized diffusion tensor
$\mathbf{I}$	Identity tensor
$\mathbf{q}$	Position vector of particle
$\mathbf{v}$	Velocity of particle
$\mathbf{x}$	Macroscopic coordinates

$\mathbf{y}$	Microscopic coordinates
$\mathcal{F}$	Geometrical factor
D	Local diffusion coefficient in fluid phase
L	Macroscopic characteristic length
l	Microscopic characteristic length
l_i	Length path travelled by particle i
N	Number of paths
Nb_c	Number of circular inclusions
R	Radius of circular inclusions
R_{max}	Maximum radius of circular inclusions
R_{min}	Minimum radius of circular inclusions
S_p	Specific surface
t	Time
u	Dimensionless concentration of tracer

1. Introduction

The diffusion of aggressive ions, moisture, gases and other aggressive agents in porous cementitious materials is central for predicting the durability of reinforced concrete (RC) structures. In the case of marine or de-icing salt environments, chloride penetration induces the corrosion of reinforcements in RC [1]. Sulphates induces the concrete degradation [2], and the reaction of carbon dioxide with dissolved hydrates coupled with moisture transfer [3] contributes to both concrete damage and steel reinforcement corrosion [4]. These phenomena affect the durability of the materials and consequently reduces the service life

of structures. The macroscopic properties of cementitious materials are linked directly to their microstructure and, more precisely, to the morphology of their pores. There are several parameters used to characterize the microstructure of cement-based materials. Porosity is one of the most used. Another essential parameter describing porous media is pore connectivity. This property directly affects the durability of cementitious materials. In fact, a high degree of pore connectivity means an interconnected porosity and consequently the aggressive agents easily penetrate into the porous network of the material. Different methods are used for studying the microstructure of cementitious materials, such as mercury intrusion porosimetry (MIP) [5], nitrogen adsorption BET [6], measurement of electrical resistivity [7], nuclear magnetic resonance [8, 9], Small-Angle scattering [10], etc. Moreover, due to the complexity of cementitious materials, the porosity and the connectivity of the pores are not sufficient to characterize their microstructure finely. Another morphological property represents a common characteristic of transport phenomena in cementitious materials, it is associated with the geometry of the pore structure. This geometry is described by two parameters: tortuosity, usually defined as the ratio of the mean effective path length of the fluid through a porous medium (L_e) and the material length (L) [11, 12] and constrictivity, usually defined as the ratio between two successive different sections of pores [5]. In recent studies [13, 14, 15, 16], the fractal theory is used to characterize the transport properties of porous media and to establish a link with geometrical parameters of microstructure such as tortuosity. These works are not interested particularly in cementitious materials, but are focused on porous media that by nature have fractal characteristics. They contribute to provide clearer answers about the general problem treated in this study in terms of identification of the geometrical parameters affecting the transport phenomena in a porous medium. Regarding cementitious materials, electrical resistivity measurements are also proposed to establish a link with the morphology of the microstructure network of cementitious materials [7, 17]. These approaches involve an empirical relationship expressing the tortuosity as a function of the volume fraction of pore entrapment. Indirect

methods, such as ultrasonic methods [18], were used to estimate the tortuosity from the measurements of reflected waves at two oblique incidence angles. However, different factors such as the geometry and the heterogeneity of the cementitious materials, the presence of steel reinforcement and moisture, make these methods less precise. Boukhatem et al [19] used a soft computing approach to predict the transport tortuosity of the pore system of fly ash concrete by building an intelligent hybrid system. In their system, a genetic algorithm was used to optimize the structure and the hyper- parameters of the network. The system presented in their study takes into account the effect of the porous network concrete in terms of porosity, and it does not consider the transport properties (permeation or diffusion), which are governed by the tortuosity and the constrictivity of the porous network. 3D reconstructions obtained by X-ray tomography were used to quantify the tortuosity and connectivity of the pores using a specific 3D-image analysis and a random walk simulation [20, 21, 22]. Authors showed that this technique provides a promising non-destructive alternative for the pore-related characterization of cementitious materials. However, cementitious materials present a very fine micro porosity at nano-metric scale and the use of such approaches is currently limited by the spatial resolution and the precision that can be obtained. Several theoretical models were also used to assess the tortuosity of cementitious porous media [23, 24, 25, 26], based on a certain model of the structure of a porous medium. However, they are very idealized. Empirical approaches have been also proposed to estimate a combination of the two parameters tortuosity and constirctivity of porous media as a function of porosity [27, 28, 29, 30]. They contain parameters determined by adjusting experimental data. In contrast, these adjustable parameters vary considerably depending on the materials used and on of their pores geometry [31], and their values reported in literature vary widely.

The effect of pore geometry on the transport properties of cement-based materials makes the problem of predicting tortuosity and constrictivity extremely complex. Indeed, it is known that cementitious materials are very heterogeneous porous media and have a complex microstructure at the microscopic and

nanoscopic scales [32]. The global behavior of these materials is then governed by local mechanisms acting at the pore scale. The major challenge consists of a better comprehension of physical phenomena that intervene at the scale of the pore, and their relation with the global behavior, all this taking into account the effect of pore geometry. The possible solution is the use of homogenization methods to describe finely these very heterogeneous media at the pore scale. One of the widely used homogenization methods in literature is the periodic homogenization method [33, 34, 35, 36, 37]. It is mainly based on the method of asymptotic developments and it assumes that the microstructure of the medium is constituted of a periodic repetition of a certain basic elementary cell. In [36] and [37], the periodic homogenization method is based on a dimensional analysis of the transport equations written on the microscopic scale, making naturally appear dimensionless numbers characterizing the problem. Recent contributions in the literature have presented asymptotic periodic homogenization studies on cementitious materials, applied to heat and moisture transfers [38, 39, 40], prediction of effective mechanical, diffusive, and chemo-expansive properties [41], diffusion-reaction problems [42], alkaline - silica reaction (ASR) [43], thermal conduction [44, 45], modeling of calcium leaching [46], and the transfers of chloride ions taking into account ionic electrocapillary interactions with the solid matrix [37, 47, 48, 49], etc. Finally, let us cite also recent works using homogenization by two scales convergence methods [50, 51]

The aim of this paper is to develop a pertinent approach to evaluate the tortuosity and constrictivity of porous media, mainly cementitious materials, by asymptotic periodic homogenization from transport equations written at the local scale for each phase of the cementitious material. The limitations mentioned above have been overcome and the effect of the pore geometry on the tortuosity and constrictivity of the material has been considered by rigorously incorporating the geometric characteristics of the microstructure. The equations of the model, developed by the upscaling micro-macro method, depend directly on the geometry of the porous medium through the homogenized parameters and the boundary value problem calculated numerically on microstructures of the mate-

rial considered. The article is organized as follows. Section 2 presents a review of the homogenized model developed by asymptotic periodic homogenization. Then, the properties of the material are calculated by numerical simulations in section 3 by solving the boundary value problem which depends on the microstructure of the material. Different geometries of the porous medium were considered for the tortuosity calculation and the constrictivity deduction. Finally, final conclusions are given in section 4.

2. Double-scale asymptotic method

The periodic homogenization method is one of many other up-scaling techniques used to describe the physical phenomena at the global scale starting from the local one. Let us consider that the porous material studied occupies the domain S of the three-dimensional space $\mathbb{R}^3$, whose characteristic length is denoted L (Fig. 1). The macroscopic domain S is limited by the boundary ∂S. A point of the macroscopic domain S will be denoted $\mathbf{x} = (x_1, x_2, x_3)$. The microstructure of the considered porous material is assumed to be periodic and constituted of the repetition of the elementary cell $\Omega = \Omega_s \cup \Omega_f$ composed of a solid phase Ω_s and a fluid phase Ω_f (Fig. 1). The characteristic length of the elementary cell is denoted l.

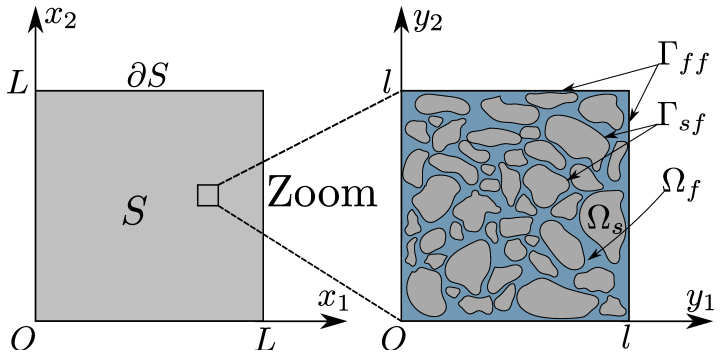

Figure 1: Description of the porous material.

The boundary of the domain Ω is noted Γ. It is composed of the solid-fluid

interface Γ_{sf} between the solid and the fluid phases and of the fluid-fluid interface Γ_{ff} separating two neighbouring elementary cells at the micro-scale. A point of the domain Ω at the elementary cell will be noted $\mathbf{y} = (y_1, y_2, y_3)$. The characteristic length of the elementary cell l must be very small compared to the macroscopic characteristic length L.

If we consider classical molecular diffusion in cementitious materials or ionic diffusion without electrical double layer effects [48], the diffusion is governed by Fick equation or Nernst-Planck equation (without charge effects) and the homogenized diffusion tensor is given by[1]

$$\mathbf{D}^{\text{hom}} = \frac{1}{|\Omega|} \int_{\Omega_f} D \left(\mathbf{I} + \left(\frac{\partial \boldsymbol{\chi}}{\partial \mathbf{y}} \right)^T \right) d\Omega \tag{1}$$

where vector $\boldsymbol{\chi}$ is periodic and of zero average on Ω_f, solution of the following boundary value problem:

$$\begin{cases} \text{div}_y \left(D \left(\mathbf{I} + \left(\frac{\partial \boldsymbol{\chi}}{\partial \mathbf{y}} \right)^T \right) \right) = 0 & \text{in} \quad \Omega_f \\ \left(D \left(\mathbf{I} + \frac{\partial \boldsymbol{\chi}}{\partial \mathbf{y}} \right) \right) . \mathbf{n} = 0 & \text{on} \quad \Gamma_{sf} \end{cases} \tag{2}$$

In (2), $\mathbf{I}$ denotes the identity tensor and $()^T$ is the transposition operator. D is the local diffusion coefficient in the fluid phase Ω_f.

In this study, the local diffusion coefficient D is assumed to be constant. The

[1] This is a classical result well established in periodic homogenization techniques whose details may be found in [48, 52].

boundary value problem (2) then simplified to:

$$\begin{cases} \Delta\chi_i = 0 & \text{in} \quad \Omega_f & \text{(3a)} \\ \dfrac{\partial\chi_i}{\partial\mathbf{y}}.\mathbf{n} = -n_i & \text{on} \quad \Gamma_{sf} & \text{(3b)} \\ \chi_i(\mathbf{y}) = \chi_i(\mathbf{y}+l) & \text{on} \quad \Gamma_{ff} & \text{(3c)} \\ \langle\chi_i\rangle = \dfrac{1}{|\Omega|}\displaystyle\int_{\Omega_f}\chi_i d\Omega & \text{in} \quad \Omega_f & \text{(3d)} \end{cases}$$

where χ_i represents the components of the vector $\boldsymbol{\chi}$ and $\langle\chi_i\rangle$ denotes the average of χ_i over Ω.

In numerous references in the literature for non reactive molecular diffusion, authors define the ratio D^{hom}/D as a geometrical factor $\mathcal{F}$ including porosity, tortuosity and constrictivity of the pore network, when the diffusion is electrically neutral, i.e. without interactions between species or at the solid-fluid interface Γ_{sf}.

We propose in this work to focus on the most common definition of the geometrical factor used in literature [53, 54, 55, 56] that is

$$\frac{D^{hom}}{D} = \frac{\varphi\delta}{\tau^2} \tag{4}$$

where φ denotes the porosity and δ the constrictivity. The relationship (4) highlights that for the particular case of a cylindrical porous network, i.e. when δ and τ are equal to 1, the ratio between D^{hom} and D is directly given by the porosity, i.e. by the reduction of the section through which the species diffuses.

The tortuosity τ of the porous medium is generally defined as:

$$\tau = \frac{\left(\frac{1}{N}\displaystyle\sum_{i=1}^{N} l_i\right)}{l} \tag{5}$$

where l_i denotes the i-th tortuous path, N is the number of paths and l is the size of the elementary cell.

To determine the length of possible paths l_i, we propose to solve the following auxiliary (dimensionless) diffusion problem posed on the elementary cell with associated homogeneous Neumann boundary conditions:

$$\begin{cases} \Delta_y u = 0 \quad \text{in } \Omega_f & \text{(6a)} \\ \dfrac{\partial u}{\partial \mathbf{y}}.\mathbf{n} = 0 \quad \text{on } \Gamma_{sf} & \text{(6b)} \\ u\left(0, y_1\right) = 1 \quad \text{on } \Gamma_{ff}\left(Inlet\right) & \text{(6c)} \\ u\left(l, y_2\right) = 0 \quad \text{on } \Gamma_{ff}\left(Outlet\right) & \text{(6d)} \end{cases}$$

where u presents the tracer dimensionless concentration. For this steady-problem, the paths (trajectories) are superimposed to the streamlines of problem (6). To determine trajectories, we solve the following equation of motion of massless particles:

$$\frac{d\mathbf{q}}{dt} = \mathbf{v} \tag{7}$$

where t denotes the time, $\mathbf{q}$ is the particle position vector of components $\mathbf{q} = (q_{y_1}\, q_{y_2})$ and $\mathbf{v}$ is the velocity function of diffusion flux streamlines obtained from the solution of problem (6) as:

$$\mathbf{v} = \left(-\frac{\partial u}{\partial y_1} \quad -\frac{\partial u}{\partial y_2} \right)^T \tag{8}$$

After the determination of the trajectories of particles, we calculate the distance travelled by each particle. Let us notice that the path number is equal to the particle number injected in Ω_f along the inlet interface Γ_{ff} where the boundary condition (6c) is imposed. Indeed, the trajectory of each particle allows to determine one value of tortuosity τ_i. The tortuosity in the considered direction is the arithmetic average of all tortuosity particles according to equation (5).
In parallel, we will solve closure problem (3) to determine vector $\boldsymbol{\chi}$ on the same elementary cell characterizing the porous network and compute the homogenized diffusion tensor $\mathbf{D}^{\mathbf{hom}}$ from equation (1). Then, from (4), we can deduce the value of the constrictivity δ for each considered porosity φ. This procedure will

be applied in the next section for different elementary cell geometries.

3. Numerical simulations and parametric study

The aim of this section is the determination of the tortuosity and constrictivity parameters on 2D elementary cells.

3.1. Case of one pore with variable size

We consider the periodic elementary cell of size $(l \times l)$, which is constituted of a solid domain Ω_s and a fluid domain Ω_f. The interface solid-fluid Γ_{sf} is defined quadratic Bézier curve of three points $(P_1\,(0,0)\,;\ P_2\,(l/2,d)\,;\ P_3\,(l,0))$ for the bottom interface and $(P_4\,(0,l)\,;\ P_5\,(l/2,l-d)\,;\ P_6\,(l,l))$ for the top interface (Fig 2). The positions of points P_2 and P_5 varies according to the variation of parameter $d \in [0.1\ \ 0.9]$ with a step of about 0.1, leading to porosities $\varphi \in [0.486\ \ 0.943]$. The finite element method is used to solve problems (3), (6) and (7).

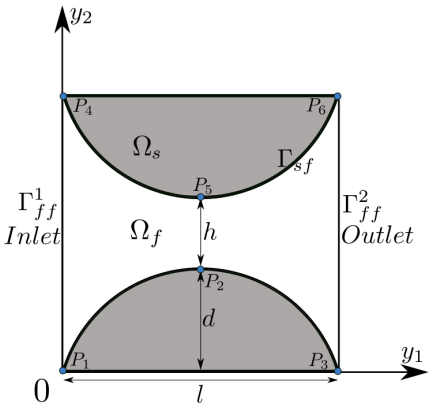

Figure 2: Description of the elementary cell.

Let us apply the numerical procedure described previously to compute the tortuosity τ. It is important to underline that according to the geometry of the elementary cell, only χ_1 is non null. Thus, we solve problem (3) for the variable

χ_1 only. The periodic boundary conditions (3c) are imposed on boundaries Γ^1_{ff} and Γ^2_{ff}.

The problem (6) is then solved in direction y_1 by imposing Dirichlet boundary conditions (6c)-(6d) on Γ^1_{ff} and Γ^2_{ff} with $u = 1$ at $y_1 = 0$ and $u = 0$ at $y_2 = l$, respectively. The Neumann boundary conditions (3b) and (6b) of problems (3) and (6) are applied on the interface solid-fluid Γ_{sf}. Figure 3(a) shows the distribution of variable χ_1.

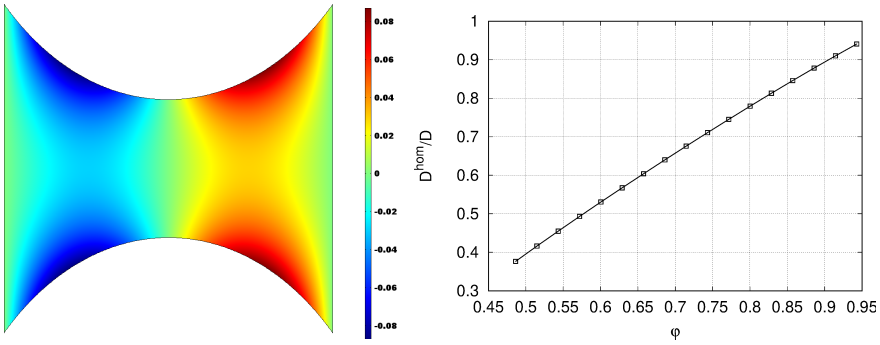

(a) (b)

Figure 3: (a) Variable χ_1. (b) Variation of relative homogenized diffusion coefficient versus porosity φ.

After solving problem (3), the homogenized diffusion tensor $\mathbf{D^{hom}}$ is determined by using expression (1) for different values of the porosity φ. Figure 3(b) shows the variation of D^{hom}/D versus porosity φ of the elementary cell of figure 2. As expected, we observe that the relative diffusion coefficient D^{hom}/D increases with the increase of the porosity.

The second step of this numerical procedure consists in solving problem (6) in order to determine u in fluid domain Ω_f (see figure 4(a)). From u, we determine the velocity vector given by expression (8). The equation of motion (7) is then solved by injecting particles on the boundary Γ^1_{ff}, which represents the inlet of particles (Γ^2_{ff} is the outlet). The number of particles injected is $N = 100$ uniformly distributed on the inlet Γ^1_{ff}. The time step is about $\Delta t = 5 \times 10^{-3}$ s,

the simulation stops when all particles reach the outlet boundary Γ_{ff}^2. Figures 4(b) and 4(c) show the trajectories and velocity magnitude of particles injected for two time values.

The determination of the elementary cell tortuosity of figure 2 in the direction

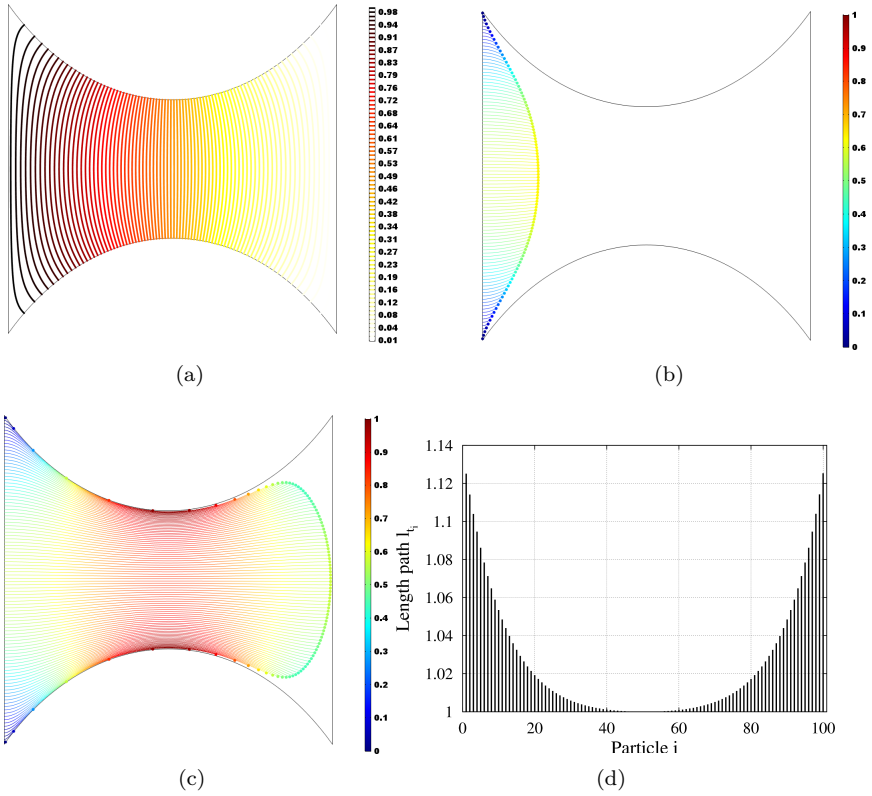

Figure 4: (a) Contours of variable u. (b) Particle trajectories at $t = 0.2\,\mathrm{s}$ and (c) at $t = 1.01\,\mathrm{s}$. (d) Path travelled by each particle.

y_1, requires the calculation of the length of each particle trajectory. For any particle i $(i = 1,\ N)$, the length of path l_i is given by:

$$\Delta l_i\,(t) \;=\; \left(\left(q_{y_1}\,(t+\Delta t) - q_{y_1}\,(t)\right)^2 + \left(q_{y_2}\,(t+\Delta t) - q_{y_2}\,(t)\right)^2\right)^{\frac{1}{2}} \qquad (9)$$

$$l_i \;=\; \sum_{t=0}^{t_f} \Delta l_i\,(t) \qquad (10)$$

where $\Delta l_i\,(t)$ is the increment of distance travelled at time t and t_f is the time required for particle i to reach the outlet Γ^2_{ff}.

Figure 4(d) shows the distance travelled by each particle. We remark that in the vicinity of the solid-fluid interface Γ_{sf} the paths are longer. Far from Γ_{sf}, the paths length becomes closer to the size of the elementary cell l. The tortuosity is finally determined from equation (5) with $N = 100$ and for different values of porosity φ (see figure 5(a)).

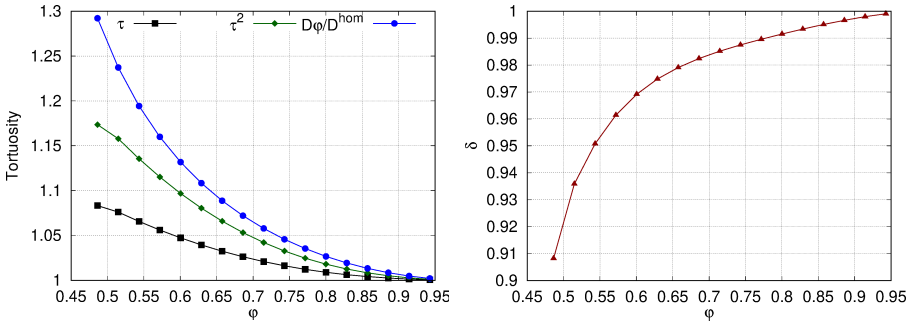

(a) (b)

Figure 5: (a) Variation of tortuosity versus porosity φ. (b) Variation of constrictivity δ versus porosity φ.

We remark that the squared tortuosity τ^2 obtained from equation (5) is lower than the ratio $\left(D\varphi/D^{hom}\right)$ derived from homogenization procedure. This means that the geometrical tortuosity effects should be completed by the constrictivity δ, accounting for shrinkage or enlargement between obstacles. All these geometrical effects are taken into account in the expression of the homogenized diffusion tensor D^{hom}. The knowledge of tortuosity τ and ratio $\left(D^{hom}/D\varphi\right)$ enables to determinate the constrictivity δ from equation (4). Figure 5(b) shows the variation of δ versus the porosity φ. We notice that δ increases with the increase of the porosity φ, even if its value is contained in the interval [0.9, 1] in the configuration studied.

3.2. Case of a circular inclusion

Let us consider an elementary cell with a circular inclusion of radius R located in the center of the periodic cell of size 1×1 (Fig 6). The radius R varies in the interval $R \in [0.05 \;\; 0.45]$ leading to a variation of the porosity in the range $\varphi \in [0.3, \;\; 0.99]$.

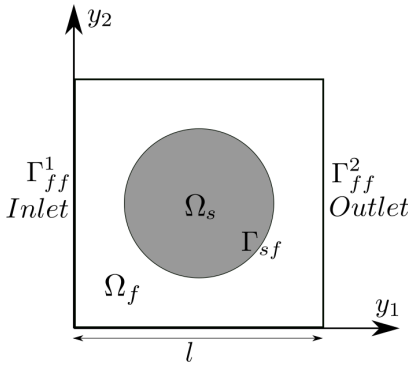

Figure 6: Elementary cell with circular inclusion.

The same procedure detailed in section 3.1 is used again for the new elementary cell considered here. Because of the geometrical symmetry of the considered unit cell, we solve problems (3), (6) and (7) only in the direction y_1. In that case the homogenized diffusion tensor is isotropic. The periodic boundary conditions are imposed on the external boundary (fluid-fluid interface Γ_{ff}) of the elementary cell. The boundary of the circular inclusion represents the fluid-solid interface Γ_{sf} where boundary conditions (3b) and (6b) are imposed. For each value of porosity φ, we solve the Neumann problem (3) and we determine the homogenized diffusion coefficient D^{hom} by using equation (1).

Figures 7(a) shows the variation of the relative homogenized diffusion coefficient D^{hom}/D versus the porosity φ. We notice that the homogenized diffusion coefficient increases with the increase of the porosity as observed in the example of section 3.1. The same result, which is intuitive, is also obtained in [48, 57].
Then, we solve problem (6) and (7) to determine the length of all possible paths

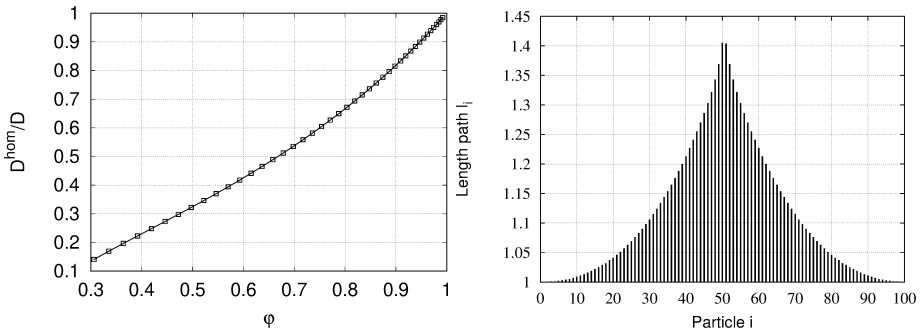

(a) (b)

Figure 7: (a) Variation of D^{hom}/D versus porosity. (b) Path travelled by each particle for $\varphi = 49.7\%$.

in direction y_1 for different values of porosity. Figure 7(b) shows the paths of 100 particles. We observe that the path length increases in the vicinity of the circular inclusion. Far from the inclusion, the paths are closer to an ideal path equal to the unit cell size $l = 1$.

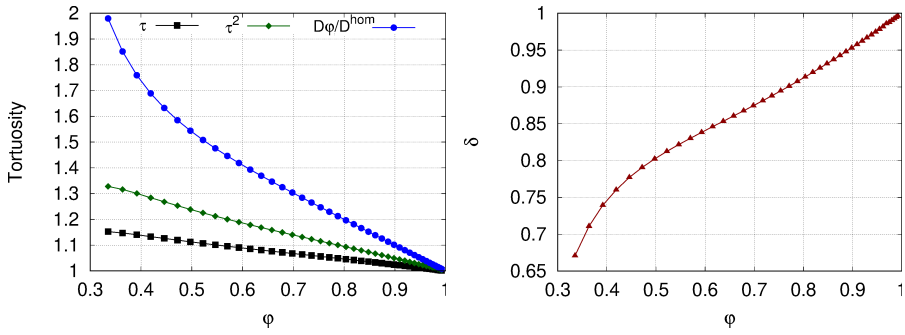

(a) (b)

Figure 8: (a) Variation of tortuosity versus φ. (b) Variation of constrictivity versus φ.

The tortuosity τ is determined from equation (5) for different values of the porosity φ. Figure 8(a) shows the variations of the tortuosity (τ and τ^2) and of the ratio $D\varphi/D^{hom}$ with respect to the porosity φ for the elementary cell of figure 6. It is important to underscore that, in the case of the circular inclusion,

the tortuosity τ follows a quasilinear behaviour with respect to the porosity φ. We notice also that the variation of the ratio $D\varphi/D^{hom}$ is non-linear for $\varphi < 0.5$. The ratio $D\varphi/D^{hom}$ increases sharply when the porosity is in the vicinity of the threshold of fluid phase connectivity ($\varphi \simeq 0.33$). We underline that the ratio $D\varphi/D^{hom}$ is higher than the squared tortuosity τ^2. The difference between $D\varphi/D^{hom}$ and τ^2 is due to the reduction of the distance between neighbouring inclusions. This effect is represented by the constrictivity factor δ according to equation (4), whose variation versus the porosity φ is plotted in figure 8(b). We observe that δ increases with the increase of the porosity, with non linear variations for porosity $\varphi < 0.5$. In this range (low value of φ), the constrictivity effect is more important because of the decrease of the distance between solid inclusions.

3.3. Case of a random porous media

In this section we are interested in the case of a random bi-dimensional porous medium (Fig 9). The periodic elementary cell, of size 1×1, is composed of discs representing the solid phase Ω_s, the domain between discs is the fluid phase Ω_f. The disc boundaries represent the solid-fluid interfaceΓ_{sf}. The external boundary of the elementary cell defines the fluid-fluid interface Γ_{ff}.

The circular inclusions are generated randomly, the radius R of each disc is chosen in the interval $R_{min} \leqslant R \leqslant R_{max}$. In addition, positions of particle centers are also determined arbitrarily in order to avoid the overlapping between discs. For that purpose, we impose that the separation distance between the centers of disc to all neighbouring ones to be smaller than a minimum distance. With this criterion, the connectivity of the fluid phase is guaranteed. The number of discs depends on the value of the fixed porosity. As a first step, we consider four values of porosity (40% 50% 60% 70%)[2]. For each porosity value, six samples

[2]Other numerical simulations with a global porosity of the sample between 8% and 20% could be performed to be more representative of porosities of classical concretes or mortars.

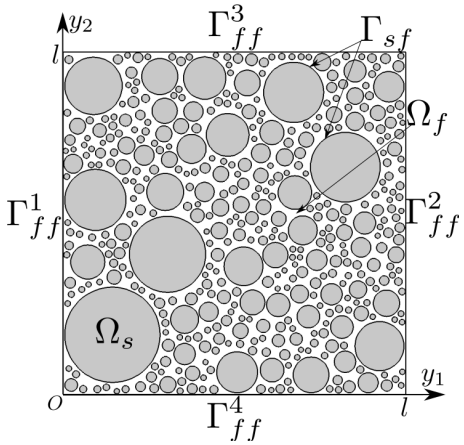

Figure 9: Periodic elementary cell of the random porous medium (bi-dimensional case).

are generated randomly. The chose of 6 samples seems to be sufficient to take into account a geometric variability. Table 1 summarizes the geometrical properties considered for the corresponding samples for all porosities. The minimum and maximum radii are fixed to be $R_{min} = R_{max}/20$ and $R_{max} = 0.15 \times l$ where $l = 1$ is the size of the unit cell. We determine for each sample the mean radius $\overline{R}$ and the standard deviation σ. Finally Nb_c denotes the number of circles necessary to reach the fixed value of the porosity.

The disc size distribution curve is presented in figure 10, for four values of the porosity. We remark for several samples that when the porosity increases, the dispersion of the size disc distribution becomes important. We observe that $\overline{R}$ and σ are closer for lowest porosity (see Table 1). Progressively, the gap increases with the increase of the porosity.

In this example, we have focused on a clearer picture of the results.

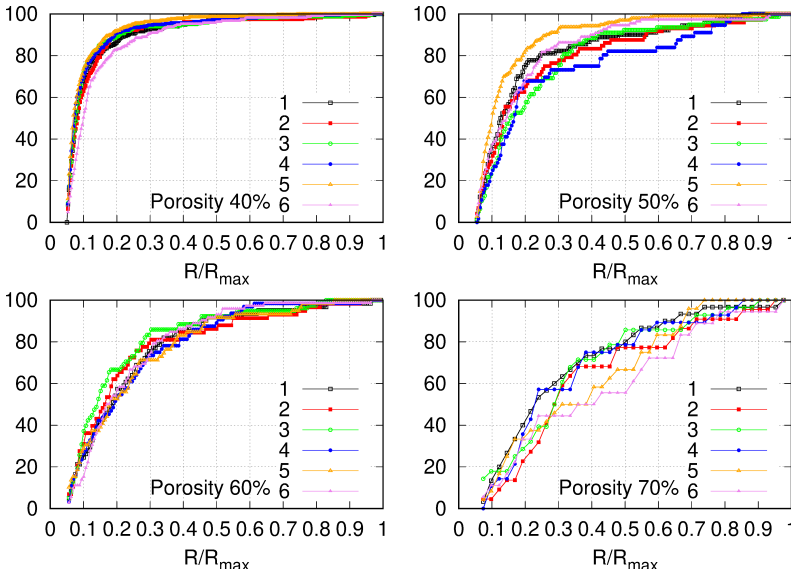

Figure 10: Grain size distribution curve for different porosities.

	$\varphi = 40\%$						$\varphi = 50\%$					
Samples	1	2	3	4	5	6	1	2	3	4	5	6
Nb_c	256	232	272	324	436	207	90	72	78	56	189	109
$\min(R) \times 10^{-3}$	7.55	7.54	7.51	7.50	7.50	7.59	7.66	7.63	7.95	8.79	7.61	7.65
$\max(R) \times 10^{-1}$	1.46	1.45	1.45	1.30	1.39	1.45	1.31	1.42	1.44	1.27	1.38	1.41
$\overline{R} \times 10^{-2}$	1.87	1.90	1.77	1.70	1.54	2.19	3.03	3.42	3.45	3.98	2.17	2.86
$\sigma \times 10^{-2}$	1.99	2.15	1.97	1.73	1.42	2.11	2.93	3.25	2.93	3.57	1.93	2.58

	$\varphi = 60\%$						$\varphi = 70\%$					
Samples	1	2	3	4	5	6	1	2	3	4	5	6
Nb_c	20	63	43	36	36	67	30	22	28	28	24	18
$\min(R) \times 10^{-3}$	7.68	7.83	12.9	8.79	7.55	7.82	7.77	10.4	7.94	10.2	9.64	9.45
$\max(R) \times 10^{-1}$	1.38	1.42	1.11	1.26	1.41	1.12	1.43	1.41	1.33	1.27	1.07	1.43
$\overline{R} \times 10^{-2}$	6.76	3.63	4.63	4.96	4.90	3.46	4.59	5.54	4.85	4.83	5.38	6.13
$\sigma \times 10^{-2}$	4.39	2.67	2.96	3.32	3.42	2.67	3.33	3.65	3.23	3.34	3.37	4.04

Table 1: Geometrical parameters of the six samples considered for each value of porosity.

As previously, we adopt the procedure outlined in section 3.1. Firstly, we solve the boundary value problem (3) in direction y_1 and y_2 to determine the components χ_1 and χ_2 of vector $\boldsymbol{\chi}$. After that, we calculate the components of the homogenized diffusion tensor using (1). In that case, $\mathbf{D^{hom}}$ is an anisotropic tensor.

In a second time, we solve the diffusion problem (6) to determine scalar variables u_1 and u_2 in direction y_1 and y_2 respectively. The periodic boundary conditions (3c) of problem (3) are applied on the external fluid-fluid interfaces Γ_{ff}. Neumann boundary conditions (3b) and (6b) of problems (4) and (6) are applied on the solid-fluid interface Γ_{sf}. In addition, boundary conditions (6b) are applied on Γ^3_{ff} and Γ^4_{ff} (Γ^1_{ff} and Γ^2_{ff}), when problem (6) is solved in direction y_1 (in direction y_2 respectively). The Dirichlet boundary conditions (6c)-(6d) are applied on Γ^1_{ff} with $u_1 = 1$ and on Γ^2_{ff} with $u_1 = 0$ in direction y_1 (on Γ^3_{ff} with $u_2 = 1$ and on Γ^4_{ff} with $u_2 = 0$ in direction y_2).

Afterwards, we solve the motion equation (7) of massless particles by injecting $N = 200$ particles on boundary Γ^1_{ff} and on boundary Γ^3_{ff} corresponding to the inlet, according to y_1 and y_2 directions. The N particles injected are uniformly distributed on the inlet boundaries and they are collected on boundaries Γ^2_{ff} and Γ^4_{ff}. The velocity of particles is then computed from the flux diffusion streamlines obtained using the gradient of variables u_1 and u_2 as follows:

$$\mathbf{v}_1 = \begin{pmatrix} -\frac{\partial u_1}{\partial y_1} \\ -\frac{\partial u_1}{\partial y_2} \end{pmatrix}; \qquad \mathbf{v}_2 = \begin{pmatrix} -\frac{\partial u_2}{\partial y_1} \\ -\frac{\partial u_2}{\partial y_2} \end{pmatrix} \tag{11}$$

The determination of the vector position from equation (7) enables to calculate the distance travelled by each particle in the two-dimensional porous medium. Finally, we determine the tortuosity using equation (5) and we deduce the constrictivity form equation (4).

We use finite element method to solve problems (3), (6) and (7). The mesh is refined in the vicinity of solid-fluid interface Γ_{sf} (Fig. 11), where the code color represents the normalized size of triangular element of the mesh.

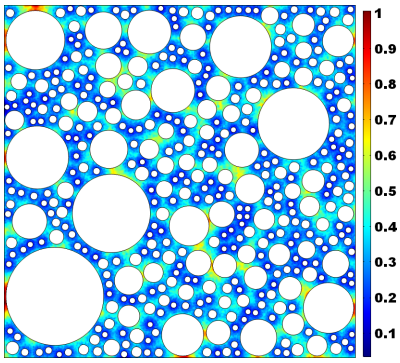

Figure 11: Mesh size distribution (the code color corresponds to the size of elements).

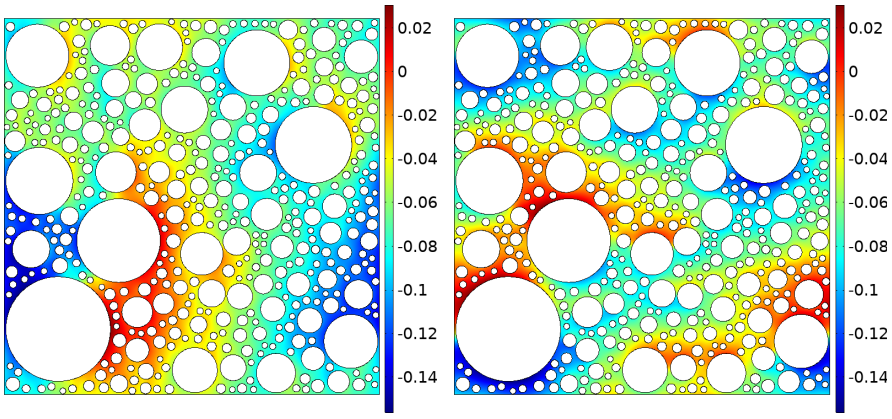

(a) (b)

Figure 12: Numerical results for the sample number 5 with a porosity $\varphi = 0.4$. (a) Distribution of χ_1. (b) Distribution of χ_2.

	$\varphi = 40\%$						$\varphi = 50\%$					
Samples	1	2	3	4	5	6	1	2	3	4	5	6
S_p	30.23	27.80	30.39	34.69	42.11	28.55	17.16	15.49	16.93	14.03	25.74	19.59
D_{11}^{hom}/D	0.216	0.204	0.211	0.212	0.223	0.212	0.283	0.271	0.302	0.317	0.275	0.294
D_{22}^{hom}/D	0.211	0.215	0.216	0.219	0.218	0.215	0.296	0.278	0.275	0.266	0.311	0.288
τ_{11}	1.177	1.173	1.171	1.158	1.163	1.159	1.128	1.117	1.116	1.119	1.141	1.130
τ_{22}	1.173	1.159	1.172	1.149	1.168	1.157	1.131	1.122	1.134	1.128	1.138	1.142
δ_{11}	0.637	0.598	0.618	0.614	0.649	0.615	0.640	0.608	0.675	0.710	0.628	0.667
δ_{22}	0.619	0.625	0.635	0.631	0.636	0.623	0.670	0.626	0.625	0.600	0.710	0.660

	$\varphi = 60\%$						$\varphi = 70\%$					
Samples	1	2	3	4	5	6	1	2	3	4	5	6
S_p	8.49	14.37	12.50	11.23	11.09	14.57	8.66	7.66	8.54	8.51	8.12	6.94
D_{11}^{hom}/D	0.369	0.400	0.388	0.374	0.353	0.383	0.487	0.461	0.511	0.494	0.493	0.546
D_{22}^{hom}/D	0.375	0.381	0.330	0.388	0.412	0.401	0.506	0.535	0.509	0.504	0.514	0.465
τ_{11}	1.100	1.100	1.093	1.102	1.117	1.107	1.068	1.092	1.094	1.076	1.072	1.063
τ_{22}	1.106	1.112	1.095	1.089	1.109	1.119	1.080	1.077	1.079	1.077	1.090	1.082
δ_{11}	0.679	0.733	0.712	0.686	0.659	0.708	0.743	0.719	0.799	0.759	0.755	0.829
δ_{22}	0.694	0.707	0.607	0.705	0.763	0.748	0.781	0.824	0.785	0.775	0.802	0.719

Table 2: Numerical results obtained on the six different samples for each value of porosity.

Figure 12(a) and 12(b) show the average[3] of components χ_1 and χ_2 of vector $\boldsymbol{\chi}$ in direction y_1 and y_2, respectively for sample number 5 with porosity of 40%. From vector $\boldsymbol{\chi}$, we calculate the components of homogenized diffusion tensor $\mathbf{D^{hom}}/D$. The numerical values of the relative diagonals values D_{11}^{hom}/D and D_{22}^{hom}/D are summarized in Table 2. We notice that the values of D_{11}^{hom}/D and D_{22}^{hom}/D present some dispersion for fixed porosity (see Fig. 13) due to the difference on the grain size distribution presented in figure 10. This dispersion becomes more important with the increase of the porosity.

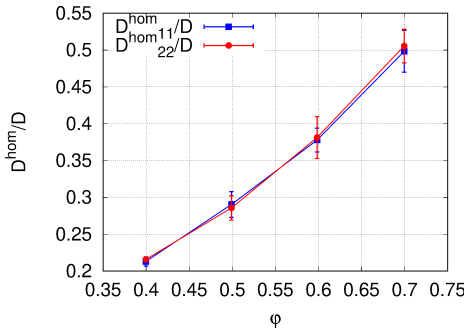

Figure 13: Variation of the mean value of the relative homogenized diffusion coefficients in direction y_1 and y_2 versus porosity. The error bar represents the dispersion (standard deviation) of the results.

The variations of the mean value and the standard deviation (error bar) of D_{11}^{hom}/D and of D_{22}^{hom}/D as function of porosity are presented in figure 13. In that case, the mean value is the arithmetic average on the samples with fixed porosity. As expected, the relative homogenized diffusion coefficients increase with φ. We observe that the mean values of D_{11}^{hom}/D and of D_{22}^{hom}/D are close due to the relatively large number of samples considered for each porosity and to the random process used. In this case, we can consider the homogenized diffusion tensor and the microstructure as (nearly) isotropic.

Figures 14(a) and 14(b) show the trajectories in the direction y_1 and y_2 respectively with a normalized magnitude velocity distribution.

[3]The average is calculated on the six samples tested and listed in table 1.

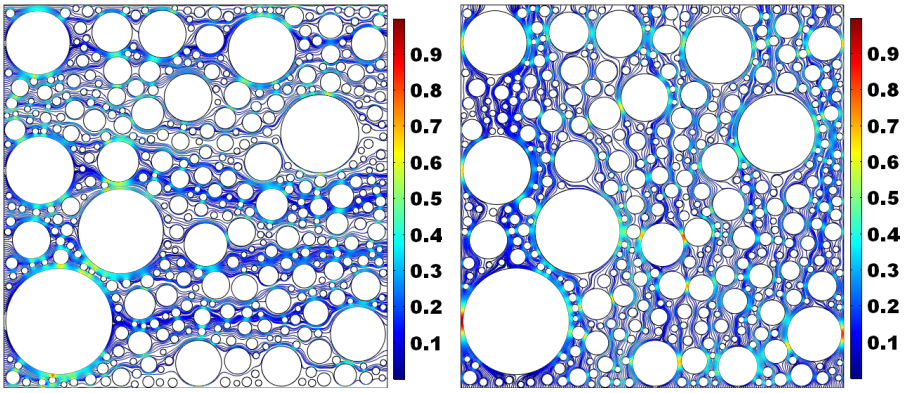

(a) (b)

Figure 14: Numerical results for the sample number 5 with a porosity $\varphi = 0.4$. (a) Particle trajectories with the normalized velocity in direction y_1. (b) Particle trajectories with the normalized velocity in direction y_2.

Tortuosity τ_{11} and τ_{22} are determined from equation (5) in the direction y_1 and y_2 respectively. These values are presented in table 2 for each sample.

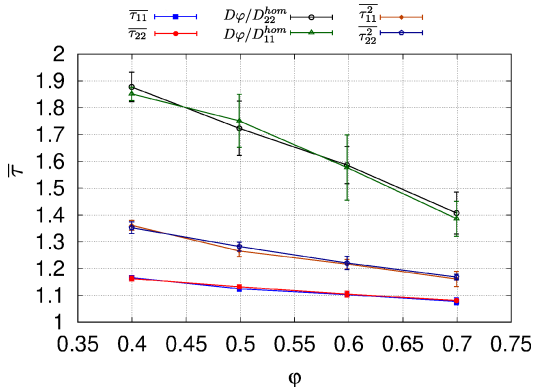

Figure 15: Variation of the mean value of the tortuosity in direction y_1 and y_2 versus porosity.

Figure 15 shows the variation of the mean value of the tortuosity $\overline{\tau}$ and $\overline{\tau^2}$ with respect to the porosity φ in direction y_1 and y_2. In the same figure, the variation of the mean values of the ratios $D\varphi/D_{11}^{hom}$ and $D\varphi/D_{22}^{hom}$ versus porosity are plotted. The difference between mean value of τ_{ii}^2 and the ratio $D\varphi/D_{ii}^{hom}$ can be quantified by the constrictivity δ_{11} and δ_{22} in direction y_1 and y_2 as in

previous cases (Table 2).

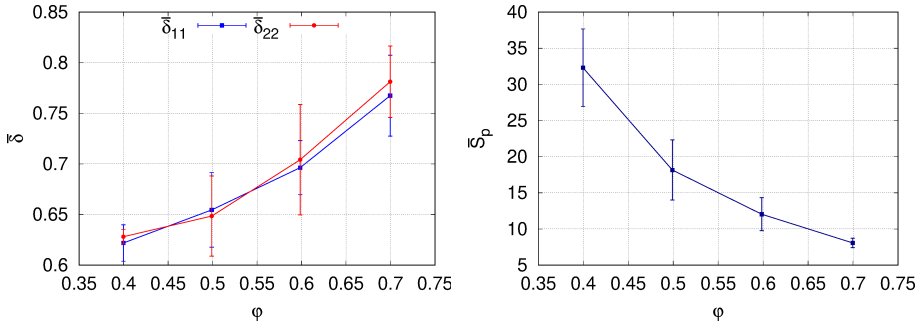

Figure 16: (a) Variation of constrictivity mean value versus porosity. (b) Variation of specific surface mean value versus porosity.

Figure 16(a) shows the variation of the average constrictivity versus the porosity in directions y_1 and y_2. We note that the constrictivities $\overline{\delta_{11}}$ and $\overline{\delta_{22}}$ increase with porosity and tend to unity for high porosity values. In addition, we observe that the constrictivity $\overline{\delta_{11}} < \overline{\delta_{22}}$, except for porosity of 50%. This is due to the variation of homogenized diffusion tensor components, which present the same behaviour in Fig. 13 (even if it is less marked). The specific surface $S_p = \dfrac{|\Gamma_{sf}|}{|\Omega|}$ takes into account the size and number of inclusions composing the numerical porous medium. For a fixed porosity, we note that the specific surface is different for different samples having the same porosity (Table 2). For a fixed value of the porosity, the specific surface presents a dispersion linked to the random way of generating the random porous medium. This dispersion is more important for smallest porosities and decreases strongly for higher porosities (Fig. 16(b)). We notice that the tortuosity increases and constricitivity decreases with the increase of the specific surface S_p. Indeed, when the discs are closer, the paths length required to bypass the solid obstacles increases. If constrictivity is considered to be the ratio of smallest to highest pore sizes, the increase of S_p leads to a pore size decrease, which corresponds to a decrease of constricivity.

3.4. Discussion and comparison

In this numerical study, we are interested in the calculation of the geometrical parameters of porous media and in the determination of the tortuosity and constrictivity with particular application to cementitious materials. The first case studied concern a unit cell constituted of a single pore with variable size. This simple geometry allowed us to highlight the effect of constrictivity and tortuosity in the diffusion process in a porous media and to extract its effect from the macroscopic ratio $D\varphi/D^{hom}$ obtained by periodic homogenization and often used in literature. These results were confirmed by the second example considered (a unit cell with a circular inclusion) where the effects of tortuosity and constrictivity are more important. In both cases, we observe the decreasing of tortuosity and the increasing of constrictivity when porosity increases. The last more complex case studied is a random porous media composed of polydisperse circular inclusions. The variation of $D\varphi/D^{hom}$ is slightly different in the two directions due to a non perfectly isotropic granular assembly. The same tendency is still observed with an amplification of the variations. In addition, the constrictivity in this case presents some dispersion due to the random way to generate the porous medium. The specific surface which takes into account the variation of the number and size inclusions, seems to have also an important effect on the constrictivity.

Let us now try to compare[4] the order of magnitude the results obtained here to some existing experimental and numerical models of the literature (Fig. 17 and 18). First, we propose to compare the ratio $D\varphi/D_{ii}^{hom}$ for random porous medium to experimental data obtained from diffusion test of chloride in cement paste. This experimental data are represented by the fitted evolution laws of the

[4]It is important to underscore that the comparison is mainly illustrative as our simulations are in 2D whereas the experimental results are obtained in 3D. Moreover, the latter have been fitted and sometimes extrapolated for a possible comparison.

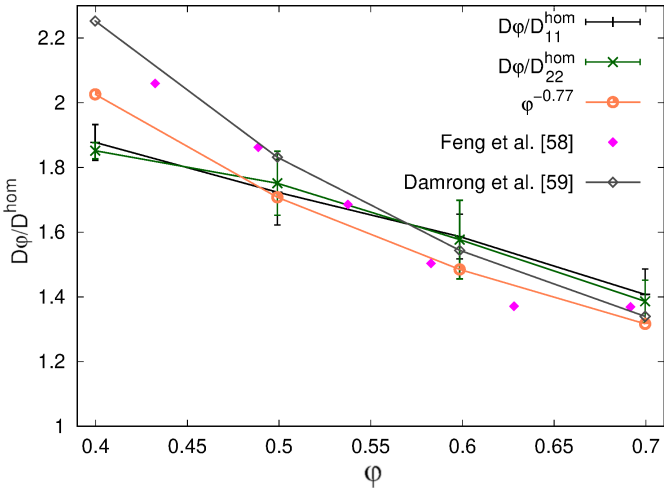

Figure 17: Comparison of $D\varphi/D^{hom}$ with experimental and numerical results in literature.

measured values. In addition, numerical models are used for this comparison as the results of Feng et al. [58] and Damrongwiriyanupap et al. [59] which give a good approximation of chloride diffusivity in cement paste. We notice that our results are of the same order as the experimental data for the high porosities, the gap becomes more important for the low porosities.

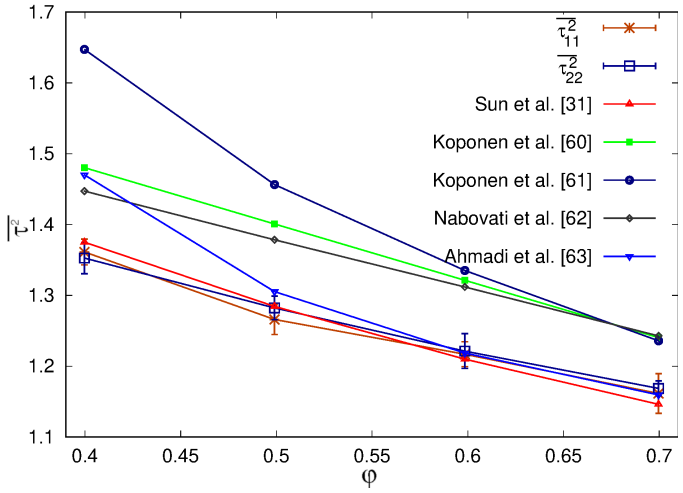

Figure 18: Comparison of $\overline{\tau^2}$ with numerical results in literature.

On Fig. 18, we compare the squared tortuosity obtained for the random porous media of Fig. 9 to the some empirical expressions obtained from numerical simulations of 2D and 3D geometry [31, 60, 61, 62, 63]. We remark that there is significant differences between our model and models of random squared overlapping inclusions [60, 61, 62]. For high porosities ($\varphi > 0.5$), our model gives squared tortuosity value closer to those obtained in the case of the cubic and tetrahedral packings of monosized spherical inclusions [63]. In the case of a circular inclusion, the model developed by Sun el al. [31], where the tortuosity is expressed with respect to porosity as $\tau = 1 - p \ln(\varphi)$, is very closer to our results with $p = 0.409$ (see equation (24) of [31]).

4. Conclusion

In this study, we presented a new approach to calculate numerically the tortuosity and the constrictivity of the pores network of a porous medium, for application to cementitious materials. In this context, the asymptotic periodic homogenization method was used to calculate a homogenized diffusion coefficient of non-reactive and non-charged particles. The latter is directly related to the geometry of the porous medium microstructure considered by means of the formation factor. It has been shown that the diffusion coefficient increases with the increase in the porosity. Then, the monitoring of particles injected in the porous network allowed calculating numerically the tortuosity of the medium. It was noted that the calculated tortuosity value is lower than the relative diffusion coefficient, which derives from the homogenization procedure. The difference is attributed to the constrictivity factor, which is deduced from this difference. In addition, the study presented in this paper aims at considering the effect of various parameters characterizing the microstructure, such as porosity, grain size distribution, specific surface of the pores and geometry of the porous medium, on the tortuosity and the constrictivity of pore network. The results indicate that:

- The values of the constrictivity evolve as the porosity. Regarding the

tortuosity, its evolution is inversely proportional to the porosity of the medium.

- The grain size distribution affects the values of the tortuosity and constrictivity of the pore network, due to the variation of the specific surface. In fact, for the same porosity, the tortuosity increases and the constrictivity of pore network decreases with the increase in the specific surface. In this case, the solid inclusions are larger and closer, they induce an increase in the paths necessary to get around the solid phase in the medium.

- For representative cells with generated inclusions, the study proved that the length of the particle path increases in the vicinity of the inclusions which oppose their trajectory. Consequently, a smaller constrictivity of the pore network and a slightly higher tortuosity were observed.

- Finally, concerning the most realistic case where the microstructure of the material is generated in a random way, the calculated tortuosity and constrictivity are different in the main directions of the medium due to the anisotropy of the microstructure.

This work provides fundamental data for a better understanding of the tortuosity and constrictivity of pore networks of complex materials. However, the geometries considered in this study allow obtaining porosities that can correspond to those of usually cement pastes and mortars. On the other hand, the case of concrete, with lower porosity (sometimes <15%), was not tackled in this study. It is therefore possible subsequently to extend this work to analyze in depth the effect the microstructural parameters governing the durability of concrete. We can consider the implementation of an approach allowing studying geometries corresponding to those of cementitious materials with very low porosities and in 3D dimensions for more realistic microstructure models.

Acknowledgements

The authors would like to express their sincere thanks to the NEEDS program for having supported this work.

References

[1] A. Aït-Mokhtar, O. Amiri, O. Poupard, P. Dumargue, A new method for determination of chloride flux in cement-based materials from chronoamperometry, Cement and Concrete Composites 26 (2004) 339–345.

[2] M. Singh, R. Siddique, A. Aït-Mokhtar, R. Belarbi, Durability properties of concrete made with high volumes of low-calcium coal bottom ash as a replacement of two types of sand, Journal of Materials in Civil Engineering 28 (2016) 04015175.

[3] M. Qin, A. Aït-Mokhtar, R. Belarbi, Two-dimensional hygrothermal transfer in porous building materials, Applied Thermal Engineering 30 (2010) 2555 – 2562. Selected Papers from the 12th Conference on Process Integration, Modelling and Optimisation for Energy Saving and Pollution Reduction.

[4] P. Turcry, L. Oksri-Nelfia, A. Younsi, A. Aït-Mokhtar, Analysis of an accelerated carbonation test with severe preconditioning, Cement and Concrete Research 57 (2014) 70–78.

[5] O. Amiri, A. Aït-Mokhtar, M. Sarhani, Tri-dimensional modelling of cementitious materials permeability from polymodal pore size distribution obtained by mercury intrusion porosimetry tests, Advances in Cement Research 17 (2005) 39–45.

[6] Q. Zeng, K. Li, T. Fen-Chong, P. Dangla, Pore structure characterization of cement pastes blended with high-volume fly-ash, Cement and Concrete Research 42 (2012) 194–204.

[7] R. He, H. Ma, R. B. Hafiz, C. Fu, X. Jin, J. He, Determining porosity and pore network connectivity of cement-based materials by a modified non-contact electrical resistivity measurement: Experiment and theory, Materials & Design 156 (2018) 82–92.

[8] Z. Hu, M. Wyrzykowski, K. Scrivener, P. Lura, A novel method to predict internal relative humidity in cementitious materials by 1h nmr, Cement and Concrete Research 104 (2018) 80–93.

[9] A. Plassais, M.-P. Pomiès, N. Lequeux, P. Boch, J.-P. Korb, D. Petit, Micropore size analysis in hydrated cement paste by nmr, Comptes Rendus de l'Académie des Sciences-Series IIC-Chemistry 4 (2001) 805–808.

[10] A. J. Allen, J. J. Thomas, Analysis of c–s–h gel and cement paste by small-angle neutron scattering, Cement and Concrete Research 37 (2007) 319–324.

[11] M. Rangelov, S. Nassiri, Empirical time-dependent tortuosity relations for hydrating mortar mixtures based on modified archie's law, Construction and Building Materials 171 (2018) 825–838.

[12] R. Zhong, M. Xu, R. V. Netto, K. Wille, Influence of pore tortuosity on hydraulic conductivity of pervious concrete: Characterization and modeling, Construction and Building Materials 125 (2016) 1158–1168.

[13] B. Xiao, S. Wang, Y. Wang, G. Jiang, Y. Zhang, H. Chen, M. Liang, G. Long, X. Chen, Effective thermal conductivity of porous media with roughened surfaces by fractal-monte carlo simulations, Fractals 28 (2020) 2050029.

[14] M. Liang, C. Fu, B. Xiao, L. Luo, Z. Wang, A fractal study for the effective electrolyte diffusion through charged porous media, International Journal of Heat and Mass Transfer 137 (2019) 365 – 371.

[15] B. Xiao, W. Wang, X. Zhang, G. Long, J. Fan, H. Chen, L. Deng, A novel fractal solution for permeability and kozeny-carman constant of fibrous porous media made up of solid particles and porous fibers, Powder Technology 349 (2019) 92 – 98.

[16] A. M. Rad, B. Ghahraman, M. Sadegh, Revising tortuosity and multifractal assumptions of unsaturated hydraulic conductivity from critical path analysis of percolation theory, Geoderma 352 (2019) 213 – 227.

[17] X. Zeng, L. Chen, K. Zheng, C. Ling, H. Zhu, H. Liu, P. Wang, K. Li, Z. Liu, M. Wang, Electrical resistivity and capillary absorption in mortar with styrene-acrylic emulsion and air-entrained agent: improvement and correlation with pore structure, Construction and Building Materials 255 (2020) 119287.

[18] Z. E. A. Fellah, S. Berger, W. Lauriks, C. Depollier, C. Aristegui, J.-Y. Chapelon, Measuring the porosity and the tortuosity of porous materials via reflected waves at oblique incidence, The Journal of the Acoustical Society of America 113 (2003) 2424–2433.

[19] B. Boukhatem, R. Rebouh, A. Zidol, M. Chekired, A. Tagnit-Hamou, An intelligent hybrid system for predicting the tortuosity of the pore system of fly ash concrete, Construction and Building Materials 205 (2019) 274–284.

[20] M. A. B. Promentilla, T. Sugiyama, T. Hitomi, N. Takeda, Quantification of tortuosity in hardened cement pastes using synchrotron-based x-ray computed microtomography, Cement and Concrete Research 39 (2009) 548–557.

[21] Z. Ranachowski, D. Jóźwiak-Niedźwiedzka, P. Ranachowski, M. Dąbrowski, S. Kudela, T. Dvorak, The determination of diffusive tortuosity in concrete specimens using x-ray microtomography, Archives of Metallurgy and Materials 60 (2015) 1115–1119.

[22] Y.-S. Wang, J.-G. Dai, X-ray computed tomography for pore-related characterization and simulation of cement mortar matrix, NDT and E International 86 (2017) 28 – 35.

[23] L. Shen, Z. Chen, Critical review of the impact of tortuosity on diffusion, Chemical Engineering Science 62 (2007) 3748–3755.

[24] M. Shafikhani, S. Chidiac, A holistic model for cement paste and concrete chloride diffusion coefficient, Cement and Concrete Research 133 (2020) 106049.

[25] R. A. Patel, Q. T. Phung, S. C. Seetharam, J. Perko, D. Jacques, N. Maes, G. D. Schutter], G. Ye, K. V. Breugel], Diffusivity of saturated ordinary portland cement-based materials: A critical review of experimental and analytical modelling approaches, Cement and Concrete Research 90 (2016) 52 – 72.

[26] Y. Dhandapani, M. Santhanam, Investigation on the microstructure-related characteristics to elucidate performance of composite cement with limestone-calcined clay combination, Cement and Concrete Research 129 (2020) 105959.

[27] M. Barrande, R. Bouchet, R. Denoyel, Tortuosity of porous particles, Analytical Chemistry 79 (2007) 9115–9121.

[28] J. Comiti, M. Renaud, A new model for determining mean structure parameters of fixed beds from pressure drop measurements: application to beds packed with parallelepipedal particles, Chemical Engineering Science 44 (1989) 1539–1545.

[29] E. Mauret, M. Renaud, Transport phenomena in multi-particle systems—i. limits of applicability of capillary model in high voidage beds-application to fixed beds of fibers and fluidized beds of spheres, Chemical Engineering Science 52 (1997) 1807–1817.

[30] L. Pisani, Simple expression for the tortuosity of porous media, Transport in Porous Media 88 (2011) 193–203.

[31] Z. Sun, X. Tang, G. Cheng, Numerical simulation for tortuosity of porous media, Microporous and Mesoporous Materials 173 (2013) 37–42.

[32] S.-Y. Chung, J.-S. Kim, D. Stephan, T.-S. Han, Overview of the use of micro-computed tomography (micro-ct) to investigate the relation between

the material characteristics and properties of cement-based materials, Construction and Building Materials 229 (2019) 116843.

[33] A. Bensoussan, J.-L. Lions, G. Papanicolaou, Asymptotic analysis for periodic structures, volume 374, American Mathematical Soc., 2011.

[34] J. B. Keller, Effective behavior of heterogeneous media, in: Statistical mechanics and statistical methods in theory and application, Springer, 1977, pp. 631–644.

[35] E. S. Palencia, Non-homogeneous media and vibration theory, Lecture Notes in Physics 127 (1980).

[36] J.-L. Auriault, P. Adler, Taylor dispersion in porous media: Analysis by multiple scale expansions, Advances in Water Resources 18 (1995) 217–226.

[37] K. Bourbatache, O. Millet, A. Aït-Mokhtar, Ionic transfer in charged porous media. periodic homogenization and parametric study on 2d microstructures, International Journal of Heat and Mass Transfer 55 (2012) 5979–5991.

[38] F. Bennai, K. Abahri, R. Belarbi, A. Tahakourt, Periodic homogenization for heat, air, and moisture transfer of porous building materials, Numerical Heat Transfer, Part B: Fundamentals 70 (2016) 420–440.

[39] W. Mchirgui, O. Millet, O. Amiri, R. Belarbi, Moisture transport in cementitious materials. periodic homogenization and numerical analysis, European Journal of Environmental and Civil Engineering 21 (2017) 1026–1042.

[40] W. Mchirgui, O. Millet, O. Amiri, Modelling moisture transport for a predominant water vapour diffusion in a partially saturated porous media, European Journal of Environmental and Civil Engineering 17 (2013) 202–218.

[41] E. Bosco, R. Claessens, A. S. Suiker, Multi-scale prediction of chemo-mechanical properties of concrete materials through asymptotic homogenization, Cement and Concrete Research 128 (2020) 105929.

[42] T. Fatima, N. Arab, E. P. Zemskov, A. Muntean, Homogenization of a reaction–diffusion system modeling sulfate corrosion of concrete in locally periodic perforated domains, Journal of Engineering Mathematics 69 (2011) 261–276.

[43] R. Rezakhani, M. Alnaggar, G. Cusatis, Multiscale homogenization analysis of alkali–silica reaction (asr) effect in concrete, Engineering (2019).

[44] K. Miled, O. Limam, Effective thermal conductivity of foam concretes: homogenization schemes vs experimental data and fem simulations, Mechanics Research Communications 76 (2016) 96–100.

[45] P. Xiao, Z. Yifeng, W. Peng, L. Dan, Estimation of thermal conduction in hollow-glass-beads-filled cement-based composites by variational asymptotic homogenization method, Applied Thermal Engineering (2019) 114191.

[46] V. Nguyen, B. Nedjar, H. Colina, J.-M. Torrenti, A separation of scales homogenization analysis for the modelling of calcium leaching in concrete, Computer Methods in Applied Mechanics and Engineering 195 (2006) 7196–7210.

[47] K. Bourbatache, O. Millet, A. Aït-Mokhtar, Multi-scale periodic homogenization of ionic transfer in cementitious materials, Heat and Mass Transfer 52 (2016) 1489–1499.

[48] K. Bourbatache, O. Millet, A. Aït-Mokhtar, O. Amiri, Modeling the chlorides transport in cementitious materials by periodic homogenization, Transport in Porous Media 94 (2012) 437–459.

[49] J. Turjanicová, E. Rohan, V. Lukeš, Homogenization based two-scale modelling of ionic transport in fluid saturated deformable porous media, Computers & Mathematics with Applications 78 (2019) 3211–3235.

[50] G. Allaire, R. Brizzi, J.-F. Dufrêche, A. Mikelić, A. Piatnitski, Ion transport in porous media: derivation of the macroscopic equations using upscaling

and properties of the effective coefficients, Computational Geosciences 17 (2013) 479–495.

[51] G. Allaire, R. Brizzi, A. Mikelić, A. Piatnitski, Two-scale expansion with drift approach to the taylor dispersion for reactive transport through porous media, Chemical Engineering Science 65 (2010) 2292–2300.

[52] K. Bourbatache, O. Millet, A. Aït-Mokhtar, O. Amiri, Chloride transfer in cement-based materials. part 1. theoretical basis and modelling, International Journal for Numerical and Analytical Methods in Geomechanics 37 (2013) 1614–1627.

[53] T. B. Boving, P. Grathwohl, Tracer diffusion coefficients in sedimentary rocks: correlation to porosity and hydraulic conductivity, Journal of Contaminant Hydrology 53 (2001) 85 – 100.

[54] T. Ishida, P. O. Iqbal, H. T. L. Anh, Modeling of chloride diffusivity coupled with non-linear binding capacity in sound and cracked concrete, Cement and Concrete Research 39 (2009) 913 – 923.

[55] J. Beaudoin, R. Feldman, P. Tumidajski, Pore structure of hardened portland cement pastes and its influence on properties, Advanced Cement Based Materials 1 (1994) 224 – 236.

[56] Q. T. Phung, N. Maes, E. Jacops, D. Jacques, G. D. Schutter], G. Ye, Insights and issues on the correlation between diffusion and microstructure of saturated cement pastes, Cement and Concrete Composites 96 (2019) 106 – 117.

[57] K. Bourbatache, O. Millet, A. Aït-Mokhtar, O. Amiri, Chloride transfer in cement-based materials. part 2. experimental study and numerical simulations, International Journal for Numerical and Analytical Methods in Geomechanics 37 (2013) 1628–1641.

[58] P. Feng, C. Miao, J. W. Bullard, A model of phase stability, microstructure and properties during leaching of portland cement binders, Cement and Concrete Composites 49 (2014) 9 – 19.

[59] N. Damrongwiriyanupap, S. Scheiner, B. Pichler, C. Hellmich, Self-consistent channel approach for upscaling chloride diffusivity in cement pastes, Transport in Porous Media 118 (2017) 495–518.

[60] A. Koponen, M. Kataja, J. Timonen, Tortuous flow in porous media, Phys. Rev. E 54 (1996) 406–410.

[61] A. Koponen, M. Kataja, J. Timonen, Permeability and effective porosity of porous media, Phys. Rev. E 56 (1997) 3319–3325.

[62] A. Nabovati, A. C. M. Sousa, Fluid flow simulation in random porous media at pore level using lattice boltzmann method, in: F. G. Zhuang, J. C. Li (Eds.), New Trends in Fluid Mechanics Research, Springer Berlin Heidelberg, Berlin, Heidelberg, 2009, pp. 518–521.

[63] M. M. Ahmadi, S. Mohammadi, A. N. Hayati, Analytical derivation of tortuosity and permeability of monosized spheres: A volume averaging approach, Phys. Rev. E 83 (2011) 026312.